ROYAL SOCIETY
OF CHEMISTRY

PAPER
Qiaoqiang Gan *et al.*
Atmospheric-moisture-driven evaporative cooling and
concurrent hydrovoltaic energy harvesting in photovoltaic
panels

Check for updates

Atmospheric-moisture-driven evaporative cooling and concurrent hydrovoltaic energy harvesting in photovoltaic panels

Sunmiao Fang, [iD] [ab] Yuxuan Huang,[a] Saichao Dang,[ab] Khalid Hazazi,[c] Yue Cao, [iD] [d] Jiachen Wang, [iD] [d] Pingfan Wu, [iD] [d] Stefaan De Wolf, [iD] [ab] Hussam Qasem[e] and Qiaoqiang Gan [iD] *[ab]

Moisture-driven hydrovoltaic devices (MHDs) are an emerging class of energy harvesters that convert ambient moisture gradients into electricity, offering notable potential for decentralized power supply in off-grid regions. However, their output performance is often limited by sluggish moisture sorption and evaporation kinetics. Herein, we developed a high-performance cellulose-based MHD that is capable of delivering a stable voltage of $\sim$0.7 V and a power density of 20 mW m^{-2} for over 30 days under ambient conditions (40%–70% RH, $\sim$20 °C). To overcome the intrinsic power limitations, we constructed a hybrid energy harvesting system by coupling the MHD with a photovoltaic (PV) panel using an interfacial hydrogel cooling layer. This synergistic design enables the MHD to harness waste heat generated by the PV panel, boosting its power output by $\sim$150%. At the same time, evaporative cooling lowers the PV panel temperature by up to 13.5 °C, increasing its power output by $\sim$15%. The integrated system can directly power various electronic devices and support energy storage, paving the way for sustainable, self-powered Internet of Things (IoT) networks and net-zero energy buildings through efficient utilization of ambient moisture and solar-induced thermal waste.

Broader context

As global demand for renewable energy grows, the efficiency and durability of photovoltaic (PV) systems are increasingly constrained by heat accumulation, which can cut electricity output by up to 20% in hot, arid regions. Passive cooling strategies, such as hydrogel-based evaporative cooling, partially mitigate this challenge but still leave most absorbed solar energy dissipated as low-grade heat. In parallel, moisture-driven hydrovoltaic devices (MHDs) have emerged as a novel technology capable of harvesting ambient moisture for decentralized power supply, yet their practical utility is hindered by sluggish moisture transport and low power densities. By synergistically integrating these two technologies, it becomes possible not only to reclaim otherwise wasted heat to enhance MHD output performance but also to suppress PV overheating and boost solar electricity output. Such a hybrid strategy addresses two long-standing challenges—thermal losses in PV modules and kinetic bottlenecks in MHDs—while offering a scalable route to self-powered internet of things networks and net-zero energy buildings. More broadly, this work illustrates how coupling ambient moisture harvesting with solar energy conversion can unlock new pathways for sustainable, all-weather energy generation tailored to extreme climates.

Introduction

Rapidly increasing global energy demand, coupled with intensifying climate pressures, is driving renewable energy systems to operate under increasingly extreme thermal conditions.[1,2] Photovoltaics (PVs), although central to the clean-energy transition, are inherently limited by severe thermal inefficiencies.[3] Typically, >70% of the solar energy incident on the PV module is dissipated as heat,[4] raising its temperature by 20–30 °C above the surrounding ambient temperature.[5] Such overheating reduces their power conversion efficiency by $\sim$0.3%–0.5% for each 1 °C increase in module temperature[6] and accelerates

[a] *Material Science Engineering, Physical Science and Engineering Division, King Abdullah University of Science and Technology, Thuwal 23955-6900, Saudi Arabia. E-mail: qiaoqiang.gan@kaust.edu.sa*

[b] *Center for Renewable Energy & Storage Technologies, King Abdullah University of Science and Technology, Thuwal 23955-6900, Saudi Arabia*

[c] *EXPEC Advanced Research Center, Saudi Aramco, Thuwal, Saudi Arabia*

[d] *Futurewei Technologies Inc., Basking Ridge, NJ, USA*

[e] *Future Energy Technology Institute, King Abdulaziz City for Science and Technology, Riyadh 11442, Saudi Arabia*

1124 | *Energy Environ. Sci.*, 2026, **19**, 1124–1136

This journal is © The Royal Society of Chemistry 2026

material degradation,[7] ultimately shortening the operational lifespan. These effects are particularly pronounced in the Middle East and North Africa, where summertime ambient temperatures often exceed 45 °C, causing PV surface temperatures to reach 70–80 °C under direct sunlight and minimal ventilation.[8] At these elevated temperatures, PV output can decline by up to 20% relative to the performance under the standard test condition of 25 °C,[6,9] undermining the economic and technical viability of solar deployment in arid climates.

To mitigate these thermal losses, passive cooling strategies have been extensively investigated.[10–13] Among them, evaporative cooling using hygroscopic hydrogel layers is especially promising due to its substantial cooling capacity.[14–16] For example, a hydrogel composed of polyacrylamide, carbon nanotubes, and calcium chloride was employed as a passive water-capturing layer for PV cooling, achieving a temperature reduction exceeding 10 °C and a cooling power of 295 W m^{-2}.[14] More recently, we developed a durable, low-cost hydrogel capable of maintenance-free atmospheric water-induced evaporative cooling, sustaining continuous operation for over one week under harsh environmental conditions in Saudi Arabia.[17] Despite these advances, the majority of solar energy absorbed by the PV-hydrogel system remains dissipated as low-grade heat—an underutilized resource that could, in principle, be reclaimed for secondary energy generation.

For effective waste-heat reclamation, PV systems can be coupled with moisture-driven hydrovoltaic devices (MHDs), an emerging class of energy harvesters that convert ambient moisture gradients into electricity.[18–20] Over the past decade, MHDs based on materials such as graphene oxide,[21,22] hydrogels,[23] polymers,[24] and composites[25,26] have been explored for sustainable, off-grid power generation, leveraging the ubiquity of atmospheric moisture.[27–30] However, their practical deployment is limited by the inherently low power densities of the materials and system design, primarily due to slow moisture kinetics.[18,31,32] Consequently, water transport and the resulting ion flux, which are critical for efficient energy conversion, are suppressed.[27]

These kinetic bottlenecks can be mitigated by strategically repurposing the waste heat that otherwise reduces PV efficiency. Most MHDs rely solely on ambient humidity gradients for electricity generation; however, introducing controlled thermal gradients can accelerate vapor diffusion and ion transport, thereby enhancing MHD electrical output performance.[33,34] Nevertheless, excessive or unregulated heating can rapidly deplete internal moisture reserves, leading to sharp performance declines. Under solar illumination, MHDs often exhibit an initial performance surge due to accelerated evaporation, followed by a rapid drop as the water content is exhausted. This instability remains a major barrier to thermally enhanced MHD operation.[35] Consequently, integrated system designs that balance thermal enhancement with sustained moisture availability are essential.

To this end, we developed a PV–hydrovoltaic hybrid system that integrates a cellulose-based MHD with a PV module via an interfacial hydrogel cooling layer. This hydrogel serves a dual role: (i) providing continuous daytime evaporative cooling to reduce PV operating temperature, and (ii) acting as a stable, all-day moisture reservoir that harnesses waste heat from the PV module to enhance hydrovoltaic electricity generation. The specially designed MHD converts ambient moisture and solar-induced waste heat into electricity through thermally assisted ion diffusion and thermogalvanic processes. Under typical nighttime conditions (40%–70% RH, ~20 °C), the MHD delivers a stable output of ~0.7 V with a power density of 20 mW m^{-2}. Solar illumination further increases the power output by ~150% through synergistic thermal–moisture coupling. Simultaneously, evaporative cooling lowers the PV surface temperature by up to 13.5 °C, improving PV electrical output by ~15%. The modular MHD architecture supports serial and parallel configurations, allowing adaptation to diverse voltage and current requirements. This versatility is demonstrated through capacitor charging and the operation of low-consumption electronics. This integrated approach provides a scalable route toward sustainable, self-powered Internet of Things (IoT) networks and net-zero energy buildings, particularly in arid, off-grid environments where efficient utilization of ambient moisture and waste heat is crucial. By addressing the dual challenges of PV thermal management and low-grade heat recovery, this study establishes a blueprint for next-generation autonomous energy systems with enhanced efficiency, durability, and adaptability.

Results and discussion

Design and fabrication of a heat- and moisture-driven power generation system

As shown in the left panel of Fig. 1, the integrated system comprises a bilayer structure on the backside of a PV panel, with a hygroscopic hydrogel as the upper layer and an MHD as the lower layer. The hydrogel passively absorbs atmospheric moisture during the nighttime and releases the stored moisture via evaporation during the daytime. This process passively cools the PV panel and supplies water vapor to the MHD, mitigating MHD performance degradation caused by rapid evaporation at elevated temperatures. The waste heat from the PV panel establishes a temperature gradient across the MHD, enhancing moisture-driven ion diffusion and driving the thermogalvanic effect in the power-generating layer. Consequently, the MHD benefits from dual enhancement: sustained moisture availability and thermally boosted hydrovoltaic electrical output.

This integrated system enables synergistic coupling among three key physical effects (right panel in Fig. 1): (i) the PV effect: solar energy is converted into electricity, while excess heat is offloaded via evaporative cooling, improving the system's energy conversion efficiency; (ii) evaporative cooling: hydrogel-mediated water evaporation lowers the PV module's operating temperature and supplies sufficient moisture to the MHD; and (iii) the hydrovoltaic effect: moisture and waste heat synergistically promote ion diffusion and trigger thermogalvanic processes in the MHD, leading to enhanced electrical output. This cooperative interaction among solar power generation, waste heat harvesting,
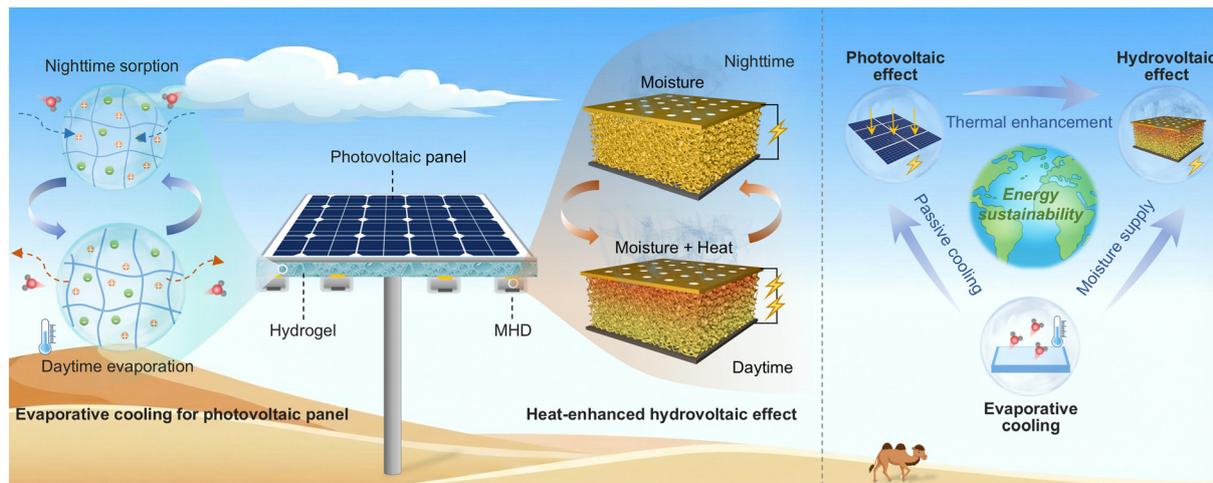
Fig. 1 Schematic of an integrated photovoltaic (PV)–hydrovoltaic hybrid energy harvesting system. The system comprises a bilayer structure with a hygroscopic hydrogel and a moisture-driven hydrovoltaic device (MHD), mounted beneath a PV panel. The hydrogel absorbs ambient moisture during the nighttime and removes waste heat from the PV panel *via* evaporative cooling during the daytime. The MHD continuously harvests ambient moisture to generate electricity and further benefits from the waste heat generated by the PV panel during the daytime to enhance its performance using the hydrogel. These coupled effects (PV effect, hydrovoltaic effect, and evaporative cooling) in the integrated system enhance its energy conversion, thermal regulation, and longevity—collectively enabling efficient, sustainable, and multifunctional energy harvesting.

and thermal regulation creates a multifunctional, self-sustained energy platform. By integrating these processes, the system addresses key challenges of PV overheating and hydrovoltaic inefficiency, offering a scalable and practical solution for continuous off-grid power generation and smart energy infrastructure.

An MHD capable of continuous and stable operation is essential to realize the proposed hybrid energy system. As shown in Fig. 2a, the design is inspired by persistent water transport in plants, where capillary action and evaporation drive directional water flow through the xylem microchannels. The persistent capillary flow within these microchannels induces directional ionic movement that establishes a streaming potential;[36] this mechanism underpins evaporation- or moisture-driven hydrovoltaic power generation.[19] Natural wood microchannels consist of cellulose chains rich in hydroxyl groups (–OH), which undergo deprotonation, electrically charging the channel surface and forming an electrical double layer,[37] accounting for the streaming potential generated within the channel.[19,38]

Mimicking this natural mechanism, we developed a cellulose-based MHD derived from natural wood. The power-generating layer is composed of cellulose modified with poly(4-styrenesulfonic acid) (PSSA), sulfuric acid (H_2SO_4), poly(3,4-ethylenedioxythiophene)/poly(styrenesulfonate) (PEDOT:PSS), and a redox couple comprising potassium ferricyanide ($K_3[Fe(CN)_6]$) and potassium hexacyanoferrate ($K_4[Fe(CN)_6]$). In this multifunctional composite, cellulose serves as the structural framework. The acidic components, PSSA and H_2SO_4, contain numerous sulfonic acid groups that provide a large reservoir of dissociable protons (Fig. S1), thereby facilitating ion transport.[39] PEDOT:PSS and the $K_3[Fe(CN)_6]/K_4[Fe(CN)_6]$ redox couple contribute to lowering internal resistance and improving the device's electrical conductivity (Fig. S2).[33] Moreover,

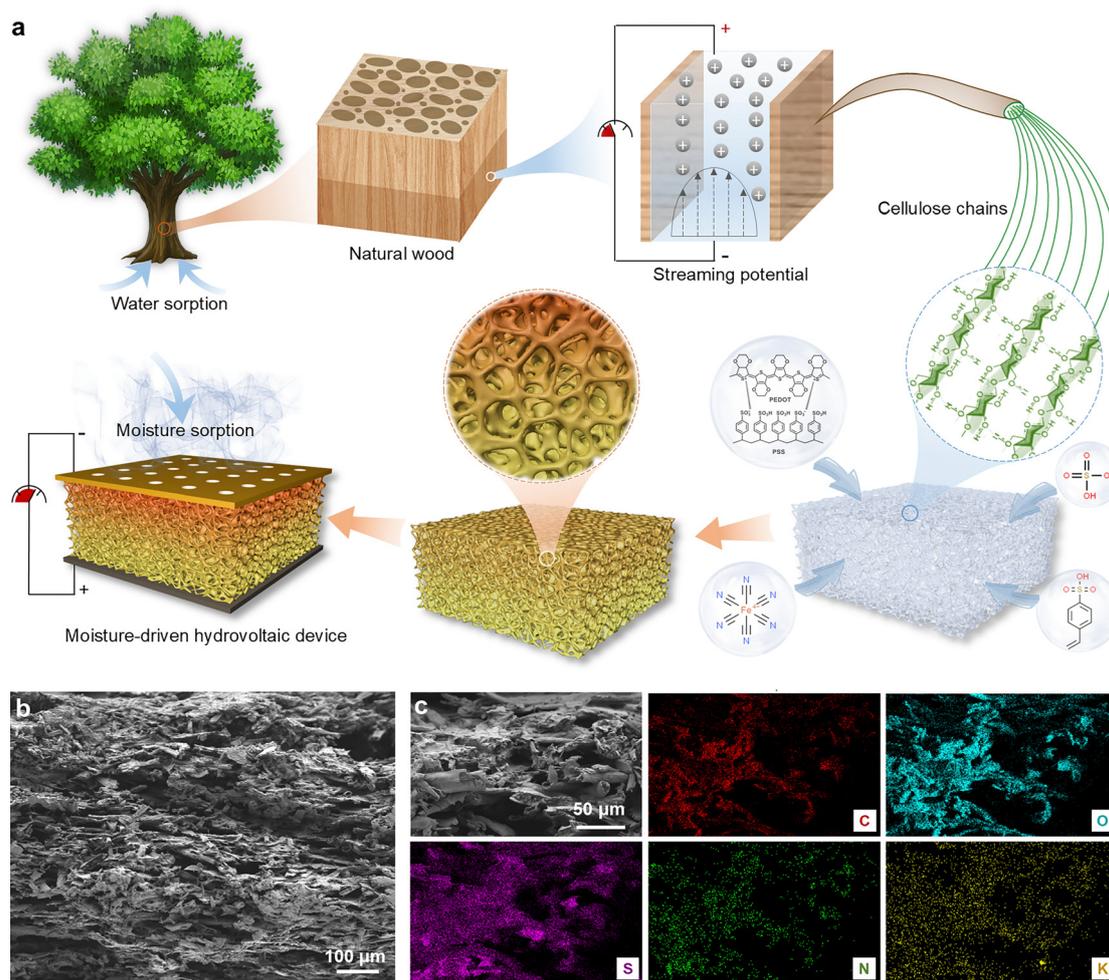PEDOT:PSS and $K_3[Fe(CN)_6]/K_4[Fe(CN)_6]$ enable conversion of thermal energy into electrical energy *via* thermal ion diffusion[40] and thermogalvanic redox reactions,[41] thereby synergistically enhancing the electrical output of the MHD. The device architecture consists of a porous gold top electrode, the multifunctional power-generating layer, and a planar graphite bottom electrode (Fig. S3). The porous gold electrode facilitates continuous moisture adsorption from the ambient environment, and the planar graphite electrode efficiently and stably collects electrons.

The MHD structure was systematically characterized. Scanning electron microscopy (SEM) images revealed a highly porous and interconnected morphology (Fig. 2b) derived from the native cellulose framework. Energy-dispersive X-ray spectroscopy confirmed the uniform distribution of key elements—including C, O, S, N, and K—across the power-generating layer (Fig. 2c), indicating successful incorporation of H_2SO_4, PEDOT:PSS, and $K_3[Fe(CN)_6]/K_4[Fe(CN)_6]$. The MHD also exhibits excellent hydrophilicity (Fig. S4), beneficial for continuous moisture uptake from the ambient environment.

Electrical output performance of the MHD

The electrical output of the MHD was systematically evaluated under varying environmental conditions. The output current markedly increased with increasing RH, indicating the critical role of ambient moisture in driving ionic transport and sustaining electricity generation (Fig. 3a). The output voltage also exhibited a similar dependence (Fig. S5), further confirming the moisture-governed nature of the device. To examine the influence of thermal input on the electrical output, a temperature gradient was applied across the membrane by heating its upper surface with a thermal pad and monitoring temperatures *via* thermocouples embedded on both sides (Fig. S6). The temperature

1126 | *Energy Environ. Sci.*, 2026, **19**, 1124–1136

This journal is © The Royal Society of Chemistry 2026

Fig. 2 Design and fabrication of a heat-enhanced MHD. (a) Bioinspired design of the MHD, mimicking natural water sorption and evaporation in plants. The power-generating layer is constructed from wood-derived cellulose and integrated with PSSA, H_2SO_4, PEDOT : PSS, and the $K_3[Fe(CN)_6]/K_4[Fe(CN)_6]$ redox couple to enable efficient ion transport and redox-assisted energy conversion. (b) Cross-sectional SEM image of the power-generating layer. (c) Elemental mapping of the power-generating layer showing the uniform distribution of elements across the membrane.
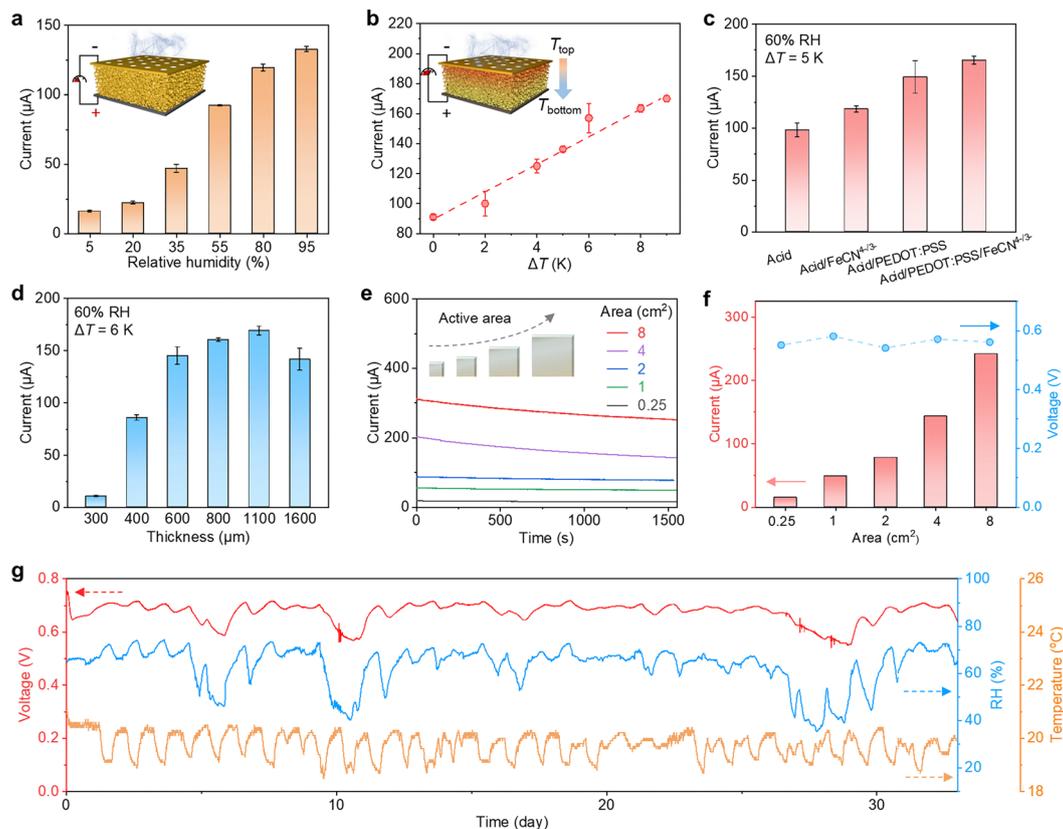
difference was defined as $\Delta T = T_{top} - T_{bottom}$, where T_{top} and T_{bottom} denote the temperatures of the top and bottom surfaces of the membrane, respectively. The output current increased consistently with ΔT (Fig. 3b), revealing a clear positive correlation between thermal input and electrical output performance. For instance, a ΔT of $\sim$9 K increased the current output by $\sim$89% from $\sim$90 μA ($\Delta T = 0$) to $\sim$170 μA. This synergistic increase arising from ambient moisture and thermal input aligned well with the dual-mode energy harvesting concept of the MHD. In addition, contributions from electrochemical reactions of the electrodes were expected to be negligible because inert gold and graphite electrodes were used.[27] Therefore, the generated electricity was considered to have originated from the combined effects of ambient moisture and thermal gradients.

The power generation performance of the MHD was systematically investigated by varying its composition. Four doping strategies were compared (Fig. 3c): (i) acid only (H_2SO_4/PSSA), providing dissociable protons;[39] (ii) acid + $K_3[Fe(CN)_6]/K_4[Fe(CN)_6]$, introducing a redox couple for thermogalvanic reactions;[41] (iii) acid + PEDOT : PSS, enabling thermally driven ion diffusion;[40] and (iv) acid + PEDOT : PSS + $K_3[Fe(CN)_6]/K_4[Fe(CN)_6]$, combining both effects.[33] Under a 5 °C thermal gradient and 60% RH, the corresponding output currents were $\sim$98, 119, 149 and 165 μA, respectively. The higher current in (ii) relative to (i) confirms the thermogalvanic contribution of $K_3[Fe(CN)_6]/K_4[Fe(CN)_6]$, whereas the enhancement in (iii) demonstrates that PEDOT : PSS facilitates thermal ion diffusion. Their integration in (iv) yields the highest current, highlighting the synergistic coupling of thermal diffusion and thermogalvanic processes.[33] These results identify a clear strategy for boosting hybrid moisture–heat energy harvesting through rational component design.

The electrical output of the MHD was influenced by both membrane thickness and area. The output current increased progressively with membrane thickness and reached a maximum at $\sim$1100 μm, after which it declined, indicating an optimal thickness of $\sim$1100 μm (Fig. 3d). In terms of active area, the device shows a pronounced increase in output with

This journal is © The Royal Society of Chemistry 2026

Energy Environ. Sci., 2026, **19**, 1124–1136 | **1127**

Fig. 3 Output performance characterization of the MHD. (a) Output current as a function of ambient RH. The current increases considerably with RH, highlighting the ability of the device for humidity-dependent energy harvesting. Inset: schematic of the MHD exposed to ambient moisture. (b) Output current as a function of the applied temperature gradient across the membrane under 60% RH. Inset: schematic of the MHD subjected to a top-down temperature gradient, mimicking solar heating conditions. (c) Comparison of the output current for cellulose membranes with varying compositions. (d) Influence of membrane thickness on the output current, showing a progressive increase with thickness and reaching a maximum at ~ 1100 μm, after which the output declines. The MHDs in (a)–(d) are 2 cm × 2 cm. (e) Output current as a function of membrane area. (f) Dependence of output current and voltage on device area, confirming size-dependent current enhancement. (g) Long-term monitoring of output voltage (red) over 30 days, alongside ambient RH (blue) and temperature (orange). The voltage remains stable at ~ 0.7 V, demonstrating excellent durability and operational robustness of the MHD over extended periods.
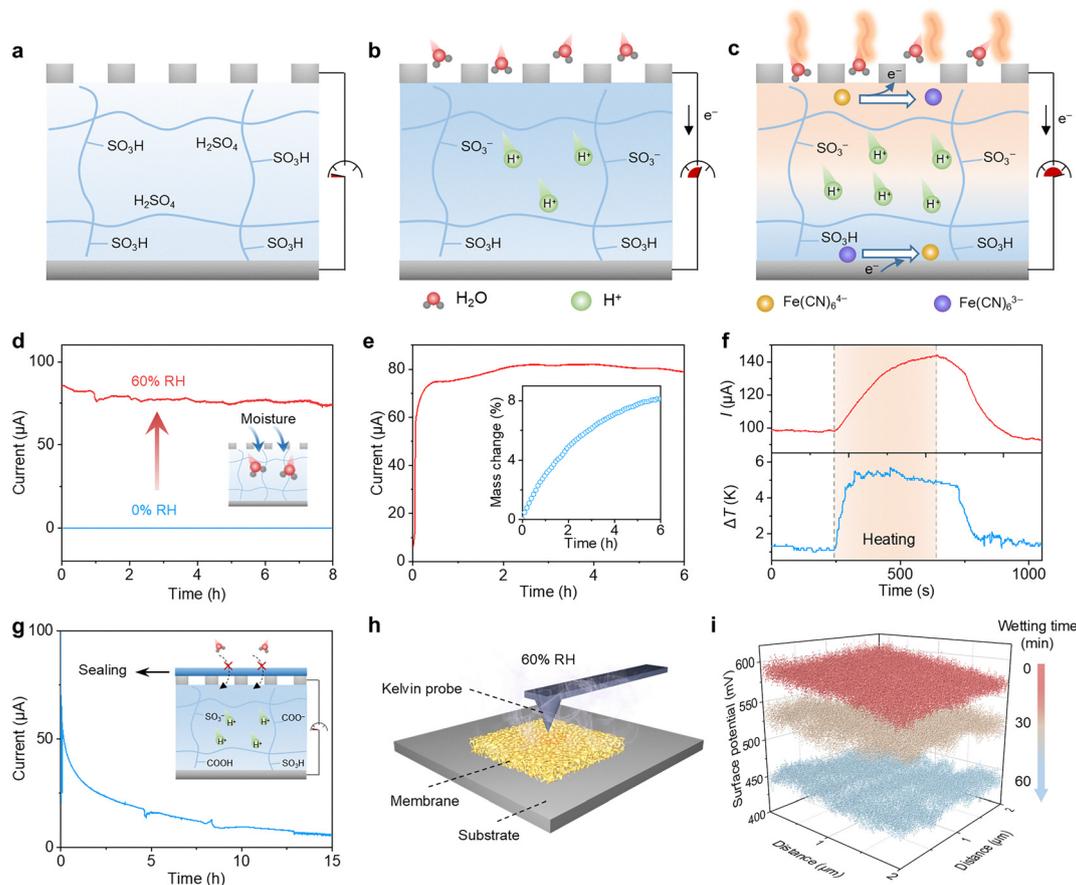
increasing area. For example, a unit with an area of 0.25 cm^2 delivered a current output of ~ 20 μA and scaling up the unit area to 8 cm^2 correspondingly enhanced the current output to ~ 240 μA (Fig. 3e). Notably, the output voltage remained largely unchanged with changes in the active area (Fig. 3f), consistent with previous studies on moisture-driven systems, indicating that voltage was predominantly determined by the interfacial potential rather than device size.[35]

The long-term operational stability of the MHD is essential for practical applications. In our experiments, a single device maintained a stable output voltage of ~ 0.7 V over 30 days under fluctuating RH (40%–70%) and ambient temperature (19–20 °C), demonstrating reliable performance under realistic conditions (Fig. 3g). Representative MHD systems reported in the literature are summarized in Table S1 and Fig. S7. The verified 30-day operation highlights the excellent stability of our device and its suitability for sustained energy harvesting applications in real-world environments. These results confirm that the integrated material design provides a robust foundation for ambient energy harvesting.

Working mechanisms of the MHD

The working mechanism of the MHD was inspired by the natural process of water transport and transpiration in plants (Fig. 2a). Evaporation at the leaf surface generates negative pressure, drawing water upward through the xylem microchannels.[37,42] These charged, narrow conduits, rich in deprotonated functional groups (such as –O$^-$), facilitate directional transport of cations (primarily H$^+$) and generate a sustained streaming potential across the channel.[42,43] Guided by this principle, an artificial membrane system was designed to mimic plant transpiration by coupling vertical water transport with ion movement (Fig. 4a–c). The MHD employs a hygroscopic matrix and proton-rich dopants (PSSA and H$_2$SO$_4$) to establish water uptake and cation transport pathways, enabling continuous moisture-driven electricity generation. Under dry conditions (Fig. 4a), humidity and ion distribution across the membrane are uniform, resulting in negligible ion migration and no detectable electrical output.[44] This baseline state was experimentally confirmed by the absence of current at 0% RH, in stark contrast to the pronounced response observed at 60%

1128 | *Energy Environ. Sci.*, 2026, **19**, 1124–1136

This journal is © The Royal Society of Chemistry 2026

Fig. 4 Mechanistic investigation of moisture-driven electricity generation. (a)–(c) Schematic of the working mechanism under different environmental conditions: (a) absence of moisture vapor, (b) presence of moisture vapor only, and (c) combined moisture vapor and thermal input. (d) Comparison of output current in dry (0% RH, blue) and humid (60% RH, red) environments, demonstrating the moisture dependence of the MHD. (e) Real-time current response of the MHD upon exposure to ambient moisture (60% RH). Inset: corresponding mass change due to moisture absorption. (f) Output current response (red curve) under an externally applied temperature gradient (blue curve). (g) Output current response when the MHD surface is sealed, confirming the role of continuous moisture absorption. (h) KPFM experimental set-up. Surface potential measurements of the power-generating layer are performed with the top surface exposed to the ambient environment (60% RH) over 0–60 min. (i) Evolution of the surface potential of the power-generating layer after 0, 30, and 60 min of moisture absorption over a $2 \times 2 \ \mu m^2$ area.

RH (Fig. 4d). When exposed to ambient humidity, the hygroscopic cellulose matrix rapidly adsorbs water, disrupting the equilibrium and initiating vertical moisture transport.[22,45] This uptake is evidenced by a progressive mass increase in the membrane ($\sim 8\%$ over 6 h; Fig. 4e, inset). Simultaneously, the incorporated proton donors (PSSA and H_2SO_4) dissociate upon moisture absorption, releasing protons *via* deprotonation of sulfonic acid groups.[39] Enhanced proton availability was validated *via* comparative pH analysis with unmodified cellulose membranes upon contact with water (Fig. S8).[24] The MHD also exhibits a more negative zeta potential than pristine cellulose, facilitating selective cation transport within the power-generating layer (Fig. S9).[46] The resulting vertical proton gradient drives directional ionic flux from the humid top surface to the sealed bottom, generating a steady internal current (Fig. 4b and Fig. S10). Correspondingly, the measured current gradually increases from 0 to $\sim 80 \ \mu A$ as moisture diffuses through the membrane at 60% RH (Fig. 4e).

When a temperature gradient is applied, the exposed top surface heats up. H^+ ions tend to diffuse from the hot side to the cold side due to the Soret effect,[40] contributing to thermopower (Fig. 4c). The direction of thermal diffusion aligns with that of moisture-driven H^+ diffusion, thereby enhancing electrical output. In addition, the temperature gradient across the membrane disturbs the equilibrium of the reversible $[Fe(CN)_6]^{3-}/[Fe(CN)_6]^{4-}$ redox couple.[33] Specifically, the oxidation reaction $Fe(CN)_6^{4-} \rightarrow Fe(CN)_6^{3-} + e^-$ occurs preferentially at the hot side (top surface), while the released electrons flow through the external circuit and are consumed at the cold side (bottom surface) *via* the reduction reaction $Fe(CN)_6^{3-} + e^- \rightarrow Fe(CN)_6^{4-}$ (Fig. 4c).[41] This thermogalvanic redox reaction generates a current that is consistent with the ionic flow induced by H^+ diffusion, further enhancing the total current. As shown in Fig. 4f, applying a 5 °C temperature difference across the power-generating layer increases the current from $\sim 100 \ \mu A$ to $\sim 140 \ \mu A$. Upon removal of the thermal gradient, the current returns to its original value, confirming that the thermal gradient synergistically enhances MHD performance. Overall, thermal diffusion and thermogalvanic redox reactions

collectively facilitate charge transfer, boosting electrical output and enabling efficient thermal–moisture hybrid energy harvesting.

The essential role of ambient moisture was further confirmed through two control experiments. When the open surface was sealed with a water-impermeable polyethylene membrane, vapor adsorption was suppressed, causing the output current to gradually drop to zero (Fig. 4g). Similarly, evacuating the surrounding air through vacuum pumping rapidly depleted the device's internal moisture, leading to a sharp decline in current. Upon re-exposure to ambient air, the output gradually recovered (Fig. S11). These results highlight the critical role of sustained ambient moisture in driving internal ion migration and maintaining continuous electricity generation.

Charge redistribution of the power-generating layer induced by ambient moisture was further analyzed using Kelvin probe force microscopy (KPFM) (Fig. 4h). As shown in Fig. 4i, the surface potential of the membrane decreased from $\sim$580 mV under dry conditions to $\sim$440 mV after 60 min of exposure to ambient moisture (Fig. S12). This potential change arises from the dissociation and downward migration of protons, leaving immobile deprotonated functional groups (*e.g.*, $-SO_3^-$) in the cellulose matrix.[30,47] The resulting electrostatic asymmetry across the membrane establishes an internal electric field, consistent with a streaming potential-like mechanism analogous to ion flow in the xylem.[37,42] Open-circuit voltage measurements of the MHD further corroborated this mechanism, identifying the bottom electrode as the anode and the top electrode as the cathode under moisture exposure (Fig. S13).[47]

In summary, the MHD operates *via* a dual mechanism: (i) moisture-driven ion transport arising from asymmetric humidity distribution, and (ii) temperature-gradient-induced thermal diffusion and thermogalvanic redox processes. These synergistic effects create a robust and sustainable platform for continuous co-harvesting of moisture and low-grade thermal energy from ambient environments.

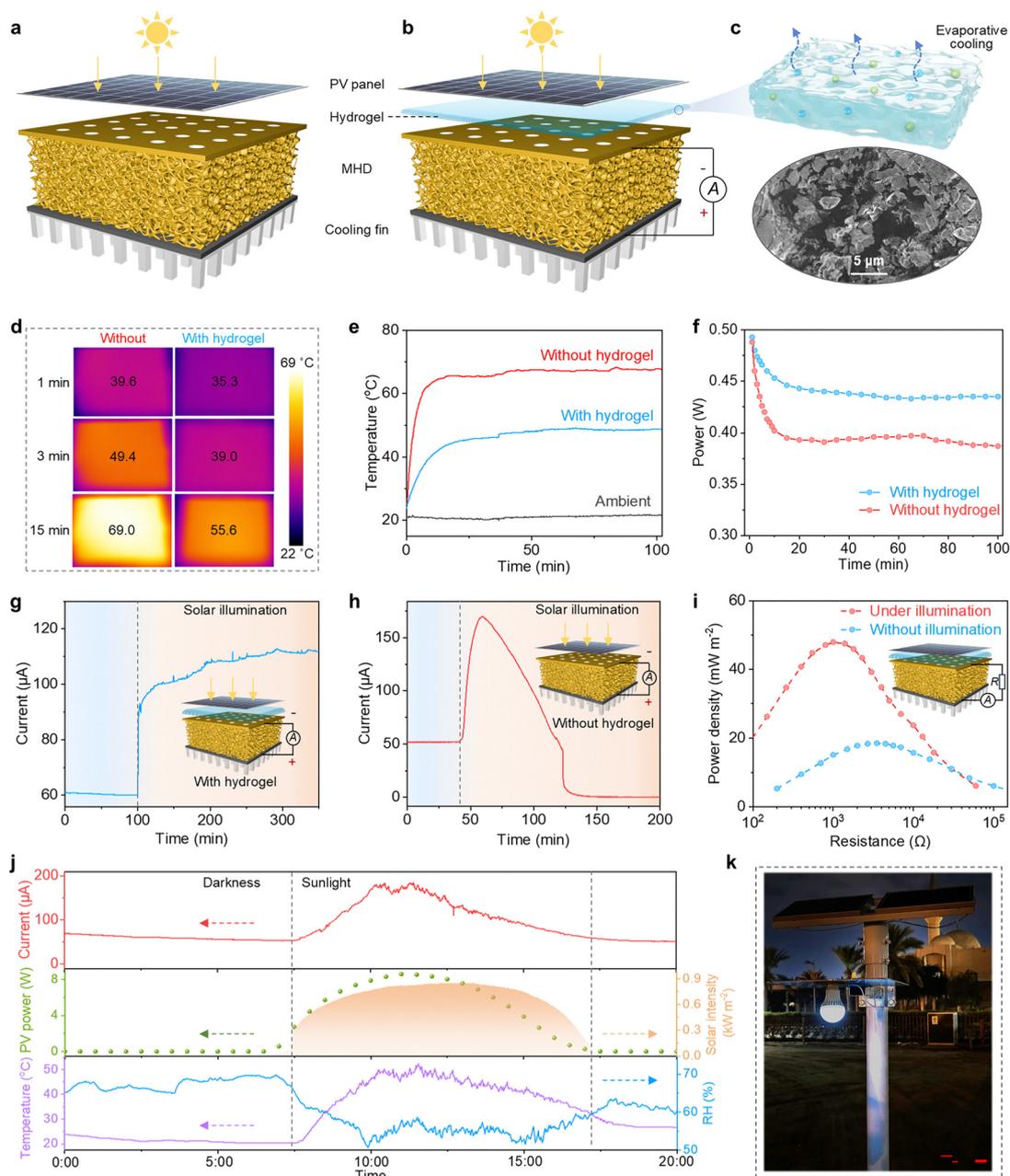## Simultaneous evaporative cooling and moisture energy harvesting integrated with PV panels

Although low-grade waste heat is abundant, it is one of the most underutilized energy sources in modern energy systems.[48] In particular, thermal losses from PV panels constitute a vast but largely untapped reservoir of low-grade heat. As discussed earlier, >70% of incident solar radiation is dissipated as heat and severely impacts the efficiency of PV modules, particularly in arid and high-irradiance regions.[3] Therefore, passive cooling strategies have been proposed, with hydrogel-based evaporative cooling showing particular promise.[14–17] Such systems effectively reduce the surface temperature of PV modules and improve their performance; however, they typically dissipate heat to the environment without further energy recovery. The proposed MHD offers a multifunctional solution by coupling evaporative cooling with active energy harvesting. By integrating an MHD with a PV panel *via* an intermediate hydrogel cooling layer, the energy harvesting system simultaneously reduced the PV panel temperature and converted waste heat and atmospheric moisture into electrical power. To our knowledge,

this is the first demonstration of a hydrovoltaic system integrated with PV modules for co-harvesting thermal and ambient energy and enhancing the overall energy efficiency of solar infrastructure. To realize this concept, a hybrid structure was designed (Fig. 5a and b). A hygroscopic hydrogel cooling layer was sandwiched between the PV panel and MHD (Fig. 5b). It thus achieved a dual functionality of passively cooling the panel *via* evaporative water loss and simultaneously supplying moisture and heat to drive the MHD. Hydrogel synthesis is detailed in the Methods section (Fig. S14 and S15), and its porous structure is evident in the SEM image (Fig. 5c). The introduction of lithium chloride (LiCl) enhanced the hygroscopicity of the hydrogel, thereby ensuring efficient and sustained water-vapor adsorption (Fig. S16). We further evaluated the thermophysical characteristics of the PAAS/LiCl hydrogel. The material shows an evaporation enthalpy of $\sim$1.81 kJ g^{-1} (Fig. S17a), a specific heat capacity of $\sim$2.31 J g^{-1} K^{-1} (Fig. S17b), and a thermal conductivity of $\sim$0.51 W m^{-1} K^{-1}, confirming efficient heat storage and transfer within the hydrated polymer–salt network. In addition, the adsorption enthalpy derived from water-vapor isotherms is $\sim$51.6 kJ mol^{-1} (Fig. S17c and d), indicating strong water binding by Li$^+$ and $-COO^-$ sites that enables continuous moisture uptake under low humidity.

The assembly of the integrated PV–MHD system follows a simple yet robust layered configuration: PV panel → hydrogel layer → MHD → cooling fin. The hydrogel layer is directly attached to the back of the PV panel through its intrinsic tackiness, requiring no additional bonding agent. The MHD itself consists of a top gold electrode, a moisture-active power-generating layer, and a bottom graphite electrode, which are mechanically fastened together at the four corners using plastic bolts, without any adhesive (Fig. S18). This configuration ensures intimate interfacial contact, minimizes additional interfacial resistance, and allows convenient disassembly or modular scale-up. In the integrated system, the same set of bolts is used to fasten both the MHD and the cooling fin through predrilled corner holes, ensuring stable mechanical compression and tight interlayer coupling (Fig. S19). This adhesive-free integration improves the reliability of interfacial thermal and mass transfer and maintains stable electrical performance over extended operation.

The electrical performance of the integrated system was evaluated under one-sun illumination using a solar simulator (1000 W m^{-2}). Infrared thermal imaging showed that the surface temperature of the uncooled PV panel rose sharply from room temperature ($\sim$20 °C) to 69 °C within 15 min (Fig. 5d). In contrast, the panel equipped with the hydrogel cooling layer maintained a considerably lower surface temperature of 55.5 °C even after 100 min of exposure, corresponding to an average cooling power in the range of 302–408 W m^{-2} (Fig. S20). Real-time temperature monitoring further confirmed that the cooled panel consistently remained markedly cooler than the uncooled one (Fig. 5e). Progressive heat accumulation in the uncooled panel caused a pronounced decline in power output over time (Fig. 5f). During an extended 400 min illumination

1130 | *Energy Environ. Sci.*, 2026, **19**, 1124–1136

This journal is © The Royal Society of Chemistry 2026

Fig. 5 Synergistic evaporative cooling and enhanced moisture energy harvesting in an integrated PV−hydrovoltaic system. (a) and (b) Schematic diagrams of the PV system without (a) and with (b) a hydrogel cooling layer. The PV−hydrovoltaic system consists of a PV panel, a hygroscopic hydrogel cooling layer, an MHD, and a cooling fin. (c) Schematic illustration (top) and SEM image (bottom) of the hydrogel cooling layer. (d) Infrared thermal images of the PV panel under one-sun illumination, showing a rapid temperature rise of the uncooled panel within the first 15 min and effective cooling by the hydrogel layer. (e) Time-resolved temperature evolution of the PV panel with and without the hydrogel cooling layer. (f) Output power of the PV panel with and without the hydrogel cooling layer. (g) and (h) Real-time current output of the MHD with (g) and without (h) the hydrogel cooling layer under one-sun illumination. (i) Power density comparison before and after solar illumination, demonstrating a synergistic performance enhancement. (j) Outdoor performance of the integrated system under real environmental conditions. (k) Photograph of the outdoor setup: 20 MHDs connected in series successfully power an LED bulb at midnight, demonstrating its potential for self-powered applications.

test, the cooled panel sustained a 13.5 °C lower temperature, achieving a ∼15% enhancement in power output relative to the uncooled panel (Fig. S21). To provide a more comprehensive comparison, additional control experiments were performed using a PV panel with an aluminium cooling fin and with both a hydrogel layer and cooling fin. After 100 min of one-sun exposure, the panel with only the fin reached 60.5 °C, while the combination of hydrogel and fin stabilized at 58.9 °C, both intermediate between the bare and hydrogel-cooled panels. The corresponding output powers followed the same trend (Table S2 and Fig. S22). These results highlight that evaporative cooling by the hydrogel layer is more efficient than conductive heat dissipation via the fins.

To benchmark the passive cooling performance, we compared the developed hydrogel–MHD system with representative sorbent-based PV thermal management systems (Table S3). Our system achieved a temperature reduction of 13.5 °C, a cooling power of 302–408 W m^{-2}, and a 15% improvement in PV output, outperforming most previously reported sorbent-based cooling materials such as PAM–CNT–CaCl$_2$ hydrogels, LiCl@ACFF composites, and k-carrageenan/PPy–LiCl beads. This comparison underscores the strong thermal management capability of our approach, which not only effectively suppresses PV overheating but also enables stable moisture supply for enhanced MHD performance.

Beyond passive thermal regulation, the hydrogel also plays a crucial role in enhancing active hydrovoltaic energy harvesting. To evaluate this function, we measured the electrical output of the MHD. Under one-sun illumination, the current output increased markedly from 60 (ambient conditions) to 110 μA (Fig. 5g). This enhancement resulted from waste heat generated by the PV panel, which induced water evaporation within the hydrogel cooling layer. The increased vapor temperature at the MHD interface and the resulting ~3 °C temperature gradient across the power-generating layer (Fig. S23) accelerated ion transport and redox kinetics, thereby boosting hydrovoltaic electricity output. In contrast, the control system without the hydrogel cooling layer exhibited poor stability: although the initial heat flux transiently increased the MHD current output, the unregulated temperature rise above 50 °C (Fig. S23) and rapid moisture loss led to device dehydration, causing a sharp and irreversible current drop to zero (Fig. 5h). This clear contrast highlights the multifunctional role of the hydrogel cooling layer in the integrated system. Specifically, the hydrogel serves two synergistic functions: (i) passively removing waste heat from the PV panel *via* evaporative cooling to enhance PV performance, and (ii) actively converting absorbed heat into evaporation enthalpy, ensuring sustained moisture release and maintaining a thermal gradient—both essential for efficient hydrovoltaic generation. Benefiting from this simple yet effective coupling strategy, the power density of the MHD under solar illumination increased 2.5-fold, from 20 to 50 mW cm^{-2} (Fig. 5i).

The practicality of the integrated system was further verified through outdoor experiments conducted in Jeddah, Saudi Arabia (March 15, 2025), with the ambient relative humidity ranging from 50% to 70%. As shown in Fig. 5j, the device generated a baseline current of ~60 μA in the absence of sunlight. Under solar irradiation, the current output gradually rose, reaching ~160 μA at peak daytime. The generated electricity could be stored in capacitors for later use, providing a potential power source for low-power electronics. As solar intensity declined toward the evening, the current returned to its baseline level, demonstrating reliable performance over a full diurnal cycle.

To further assess the applicability of the PV–hydrovoltaic system in arid regions, additional experiments were conducted under both controlled indoor and outdoor desert environments. In a low-humidity chamber (~22% RH, ~24 °C), the PV panel with the hydrogel cooling layer stabilized at 48 °C under one-sun illumination (Fig. S24), compared to

58 °C at 60% RH, indicating that lower ambient humidity enhances evaporative cooling by accelerating water evaporation. As a result, the hydrogel-cooled PV showed a 21.4 °C lower operating temperature and an approximately ~18.4% increase in electrical power output relative to the uncooled panel. The corresponding MHD current was initially limited (~7 μA) due to the low moisture content in air, but gradually increased to ~50 μA upon illumination, driven by hydrogel-derived vapor and the thermally induced gradient across the power-generating layer. Furthermore, an outdoor field test was conducted in Jeddah, Saudi Arabia (October 17, 2025), where the minimum daytime RH dropped to 11.2% and the peak temperature reached 38 °C. Under this hot–arid condition, the hydrogel-cooled PV panel maintained a temperature reduction of ~8.5 °C and delivered an average power output ~5% higher than the bare panel (Fig. S25). The MHD also operated continuously, with the daytime output current increasing from ~25 to ~140 μA, owing to sustained water-vapor release from the hydrogel and the derived thermal gradient. These results demonstrate that the integrated system remains effective and operational even under extremely low-humidity and high-temperature conditions typical of desert climates. We also performed a detailed thermal-resistance analysis (Fig. S26) and numerical simulations (Fig. S27) of the bare and hydrogel–MHD integrated PV systems, which confirm that the introduced evaporative pathway becomes the dominant additional cooling mechanism and reduces the PV operating temperature.

As a proof of concept, the assembled system successfully powered a light-emitting diode (LED) bulb at night (Fig. 5k), underscoring its potential for sustainable off-grid energy applications. Importantly, the MHD module used here is structurally identical to the units described in the following section, enabling seamless transition from a hybrid PV–MHD system to scalable modular deployment. This modularity allows the same MHD components to be used either as integrated elements beneath PV panels or as independent power units for broader applications.

Scalable applications

Building on the demonstrated hybrid PV–MHD concept, the scalability and integration potential of the MHD system with other applications were systematically evaluated. The same MHD units used in the PV-integrated device (Fig. 5) were reconfigured in various series and parallel arrangements to demonstrate modular power scaling and application versatility. To achieve higher voltage outputs, 20 MHDs were connected in series to form an integrated module (Fig. 6a). This setup yielded a total open-circuit voltage of 13.9 V (Fig. 6b), showing a near-linear increase with the number of connected devices: a single MHD generated ~0.66 V, while 5, 10, and 15 series-connected MHDs produced ~3.5, 7.05, and 10.6 V, respectively (Fig. 6c). In addition, the stacked module maintained a stable voltage output for over 36 h under ambient conditions, demonstrating excellent electrical and environmental stability—both essential for long-term use. The circuit configuration of the integrated 20-unit array is shown in Fig. S28.

The energy-storage capability of the MHD system was also evaluated by charging capacitors with a four-cell module

1132 | *Energy Environ. Sci.*, 2026, **19**, 1124–1136

This journal is © The Royal Society of Chemistry 2026

(four MHDs connected in series) that delivered a total output of ~2.5 V (Fig. S29). As shown in Fig. 6d, capacitors with capacitances ranging from 470 to 2000 µF were charged within 100 s, demonstrating the practicality of MHDs as a stable, self-powered source for driving energy-storage components. The charging voltage could be further increased by adding more cells in series (Fig. S30). The effect of modular parallelization on current output was also investigated. As shown in Fig. 6e, parallel connections of 2, 4, 8, and 10 MHDs

produced progressively higher output currents of ~45, 80, 106, and 135 µA, respectively, confirming that parallel connection is an effective strategy for current amplification (Fig. 6f). These findings highlight the modular tunability of the MHD system, allowing easy adaptation to various voltage and current requirements by reconfiguring the number and arrangement of devices.

To explore the practical utility of the developed system, we demonstrated a series of indoor and outdoor applications using
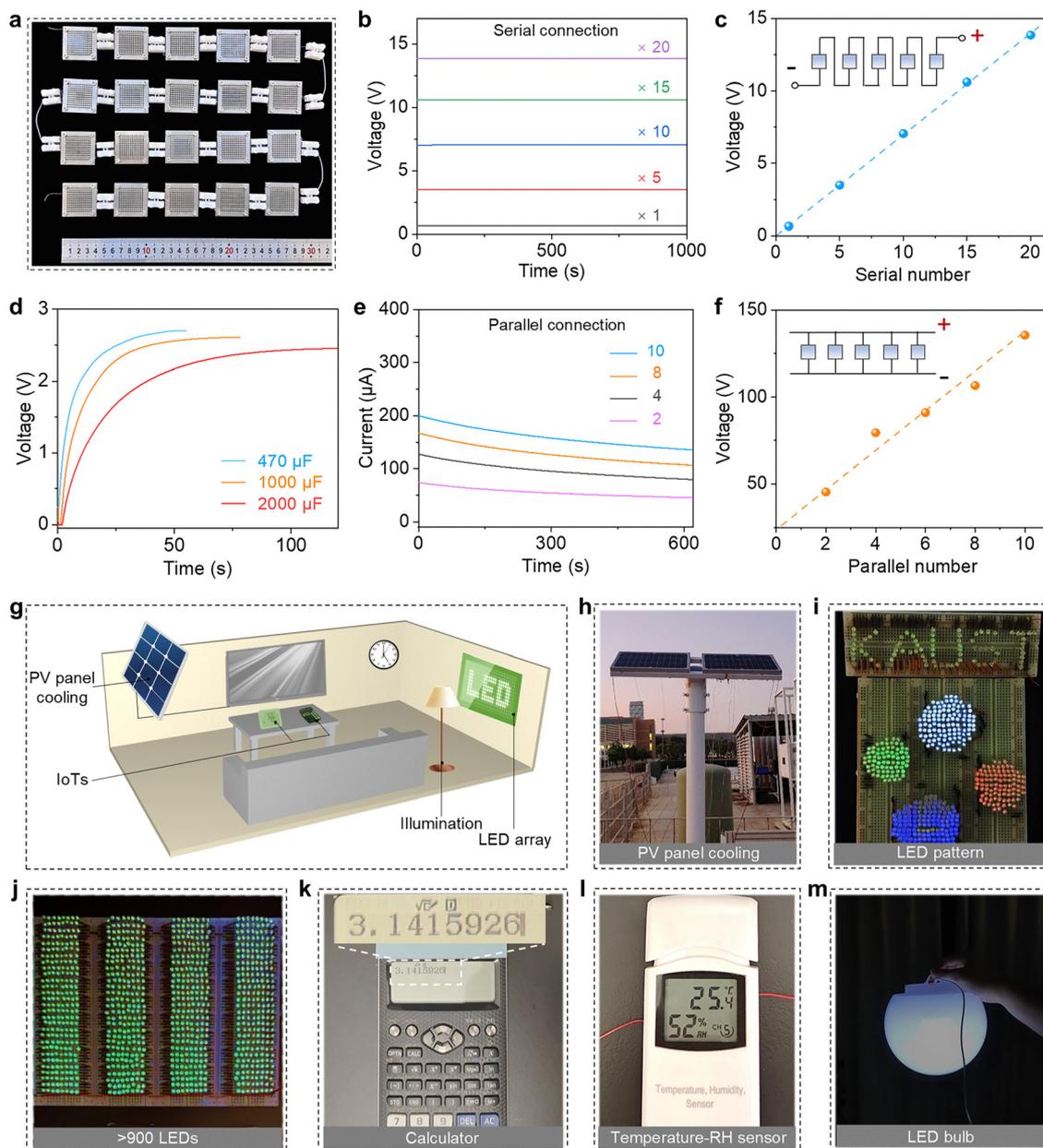
Fig. 6 Scalability and practical applications of the MHDs. (a) Photograph of an integrated array containing 20 MHDs. (b) Output voltage of the array with MHDs connected in series, demonstrating voltage amplifying capability. (c) Output voltage distribution with respect to the number of MHDs connected in series. (d) Real-time voltage profile of capacitors charged by the MHDs, validating energy storage potential. (e) Output current of the system with MHDs connected in parallel. (f) Output current as a function of the number of integrated units, confirming scalable current enhancement. (g) Conceptual schematic of a smart building powered by an integrated PV−hydrovoltaic system. (h)−(m) Demonstrated real-world applications of the MHDs: (h) PV panel cooling, (i) powering a multicolor LED pattern, (j) illumination of over 900 LEDs, (k) charging a calculator, (l) powering a temperature and humidity sensor, and (m) lighting an LED bulb, showcasing the potential of the system for installation in IoT infrastructure and net-zero energy buildings.

This journal is © The Royal Society of Chemistry 2026

Energy Environ. Sci., 2026, **19**, 1124–1136 | **1133**

the MHD modules (Fig. 6g–m). Beyond outdoor PV panel cooling (Fig. 6h), the MHDs were able to directly power electronic devices. For instance, five individual modules (each comprising four MHDs connected in series) were used to drive a multicolor LED pattern, with each module independently powering a distinct color segment (Fig. 6i and Video S1). As shown in Fig. 6j, a single 20-unit series-connected MHD module successfully illuminated over 900 LEDs simultaneously, highlighting the high-voltage capability of the assembled device (Video S2). The detailed characterizations of these two representative demonstrations are shown in Fig. S31 and S32. The system also demonstrated the capacity to power a digital calculator display (Fig. 6k and Video S3), a temperature and humidity sensor (Fig. 6l and Video S4), and an LED bulb (Fig. 6m and Video S5). Notably, the same MHD module used for the LED bulb was also deployed in the outdoor experiment shown in Fig. 5k, providing a consistent demonstration of the developed system's utility for nighttime or off-grid lighting, such as in outdoor or emergency scenarios.

These findings highlight the versatile and scalable nature of the MHD system. Owing to their modular architecture, the MHD units can function either as integrated components in hybrid PV–MHD configurations or as standalone modules, offering exceptional flexibility in system design and deployment. Their ability to harvest ambient moisture and waste heat makes them well suited for decentralized and sustainable energy applications, including distributed sensor networks, building-integrated PVs, and IoT systems. A detailed cost analysis (Table S4) was further conducted to assess the techno-economic feasibility of the integrated system. The stand-alone MHD module costs approximately \$36.8 m^{-2}, while integration with the hydrogel cooling layer and aluminum fin increases the overall material cost to \$75.2 m^{-2}. All components are fabricated from abundant, low-cost materials such as cellulose, polyacrylate, and LiCl, without external energy input. Considering the passive operation, zero-energy consumption and 15% PV efficiency enhancement achieved *via* this system, the cost–performance ratio of the system is highly favorable for large-area deployment in building-integrated or off-grid applications. Integration with advanced energy management circuits and complementary energy harvesting technologies (*e.g.*, evaporation-induced electricity[49,50] and concentrated solar thermoelectric power[51]) could further expand the power supply for a broad range of electronics.

Conclusions

In summary, we developed a multifunctional hybrid energy harvesting system by integrating cellulose-based MHDs with PV modules through an interfacial hydrogel cooling layer. The MHD delivered a stable voltage of $\sim$0.7 V with a power density of 20 mW m^{-2} for more than 30 days under ambient conditions (40%–70% RH, $\sim$20 °C). When coupled with PV panels, the system harnessed solar-induced thermal waste to boost MHD power output by $\sim$150%, while evaporative cooling simultaneously reduced the PV surface temperature by up to 13.5 °C,

resulting in a $\sim$15% increase in PV power output. The modular architecture allows straightforward scaling through series and parallel MHD connections, enabling tailored voltage and current outputs for diverse scenarios. The integrated platform successfully powered various electronic devices and supported energy storage, highlighting its potential for self-sustained IoT infrastructures and net-zero energy buildings, particularly in arid and off-grid environments. Further optimization of hydrogel composition, ion-selective functional materials, and device encapsulation strategies may extend operational humidity ranges, enhance durability, and improve conversion efficiency. By synergizing hydrovoltaic electricity generation with PV thermal management, this work paves the way for practical deployment of next-generation autonomous energy systems.

Experimental

Materials

PSSA solution (M_w 75 000, 30 wt% in H$_2$O), H$_2$SO$_4$ solution (20 wt% in H$_2$O), K$_3$[Fe(CN)$_6$], K$_4$[Fe(CN)$_6$], and methyl orange were purchased from Aladdin Scientific Corp., Shanghai, China. PEDOT:PSS was purchased from Jiangsu XFNANO Materials Tech Co., LTd, China. Lithium chloride (LiCl) and sodium polyacrylate (PAAS, M_w 5 000 000–7 000 000) were purchased from Macklin (China). The cellulose membrane was purchased from Zhongshan Nanofiber Material Co., Ltd (China). All chemical reagents were used as received without further purification.

Preparation of the power-generating layer

H$_2$SO$_4$ solution (20 wt% in H$_2$O) was first diluted to 5 wt% with deionized water. The diluted solution was then mixed with the PSSA solution at a mass ratio of 1:1. Then, the mixture was combined with PEDOT:PSS and K$_3$[Fe(CN)$_6$]/K$_4$[Fe(CN)$_6$] in a mass ratio of 90:8:1:1 and stirred vigorously for 2 h. Cellulose membranes were cut to the desired dimensions and immersed in the mixed solution for 12 h. Finally, the membranes were dried under ambient conditions (20 °C and 60% RH) for 12 h.

Fabrication of MHD

A 1-mm-thick stainless-steel plate with uniformly distributed 1.5-mm-diameter holes was fabricated and subsequently coated with a $\sim$50-nm-thin gold layer *via* magnetron sputtering to serve as the top electrode (Fig. S3). A graphite plate of the same thickness (1 mm) was used as the bottom electrode. The power-generating layer was then sandwiched between these two electrodes.

Electrical measurement of the MHD

The bottom and top electrodes were connected to the positive and negative terminals of a source meter (Keithley 2450), respectively. The open-circuit voltage was recorded under zero applied current (I = 0 mA), and the short-circuit current was measured under zero applied voltage (V = 0 V).

1134 | *Energy Environ. Sci.*, 2026, **19**, 1124–1136

This journal is © The Royal Society of Chemistry 2026

Preparation of the hydrogel

LiCl was dissolved in deionized water at a mass ratio of 1:1.5 under vigorous stirring and then cooled to room temperature. Then, PAAS powder was added to the LiCl solution at a mass ratio of 2:1 (PAAS:LiCl) and stirred for 3 min. The resulting mixture was poured into a culture dish and allowed to stand for 1 h; then, the PAAS/LiCl hydrogel was peeled off. The hydrogel was finally cut to the desired dimensions and attached to the backside of the PV panel.

Electrical conductivity measurements

The electrical conductivity σ of the sample was calculated as follows:[33]

$$\sigma = \frac{L}{R \times S} \qquad (1)$$

where L is the sample thickness, R is the resistance, and S is the cross-sectional area. The thickness was determined using a thickness gauge (De Zhi 211–561), and the resistance was measured using a digital multimeter (Keithley DMM 6500).

Cooling power evaluations

The average cooling power P_{evap} of the hydrogel cooling layer was calculated as follows:[14]

$$P_{\text{evap}} = \frac{\Delta H_{\text{evap}} \times \Delta m}{t \times A} \qquad (2)$$

where ΔH_{evap} is the enthalpy of vaporization of water, Δm is the mass change of the hydrogel cooling layer due to water evaporation loss, t is the test time, and A is the surface area of the hydrogel cooling layer.

Characterizations

The morphology and structure of the samples were examined using a ZEISS Sigma 300 scanning electron microscope. KPFM was performed using a Bruker dimension icon scanning probe microscope. The surface functional groups were characterized using Fourier transform infrared spectroscopy (Nicolet iS20). The contact angles were measured using a contact angle meter (DSA100E). Zeta potentials were determined using a zeta potential analyzer (Zetasizer Nano ZS). Evaporation enthalpy and heat capacity were measured using differential scanning calorimetry (Discovery DSC 250). Water vapor adsorption isotherms were measured using a simultaneous thermogravimetric and differential scanning calorimeter (STA 449 F3). Thermal images of the PV panel were captured with an infrared thermal camera (Fluke TiX580). Changes in the hydrogel and MHD weights were monitored with a precision mass balance (ML303T; accuracy ±0.0001 g). Indoor solar-illumination experiments were performed under laboratory conditions (20 °C and 60% RH) using a solar simulator (Newport 94043A). The real-time temperatures of the PV panel and MHD were recorded using a multichannel thermocouple thermometer (AZ88598). The output power of the PV panel was measured using a PV analyzer (PROVA 200A). Ambient temperature and humidity were monitored with a temperature–humidity meter (TH22R-EX).

Author contributions

Q. G. conceived the ideas. S. F. designed the experiments. S. F. and Y. H. performed the experiments. Q. G. and S. F. wrote the manuscript. All authors discussed the results and commented on the manuscript.

Conflicts of interest

There are no conflicts to declare.

Data availability

All data that support the conclusions of this study are present in this paper and the supplementary information (SI). Supplementary information: materials and methods. See DOI: https://doi.org/10.1039/d5ee05530j.

The data that support the findings of this study are available from the corresponding author upon reasonable request.

Acknowledgements

Notes and references

1 Approximately 100 million households rely on rooftop solar PV by 2030, https://www.iea.org/reports/approximately-100-million-households-rely-on-rooftop-solar-pv-by-2030).

2 Snapshot of Global PV Markets 2025, https://www.solareb2b.it/wp-content/uploads/2025/06/Snapshot-of-Global-PV-Markets_2025.pdf).

3 A. Khan, P. Anand, S. Garshasbi, R. Khatun, S. Khorat, R. Hamdi, D. Niyogi and M. Santamouris, *Nat. Cities*, 2024, **1**, 780–790.

4 C. Ballif, F.-J. Haug, M. Boccard, P. J. Verlinden and G. Hahn, *Nat. Rev. Mater.*, 2022, **7**, 597–616.

5 L. Xu, W. Liu, H. Liu, C. Ke, M. Wang, C. Zhang, E. Aydin, M. Al-Aswad, K. Kotsovos, I. Gereige, A. Al-Saggaf, A. Jamal, X. Yang, P. Wang, F. Laquai, T. G. Allen and S. De Wolf, *Joule*, 2021, **5**, 631–645.

6 S. Dubey, J. N. Sarvaiya and B. Seshadri, *Energy Procedia*, 2013, **33**, 311–321.

7 L. Xu, E. Aydin, M. De Bastiani, M. Babics, J. Liu, R. Azmi, M. Alamer, M. F. Salvador, W. Liu, T. Allen, F. Xu, J. Kang, A. Subbiah, W. Yan, A. U. Rehman, L. Zhou, W. Raja, Q. Gan, Z. Liu and S. De Wolf, *Adv. Energy Mater.*, 2023, **13**, 2300013.

8 E. Skoplaki and J. A. Palyvos, *Sol. Energy*, 2009, **83**, 614–624.

9 J. Adeeb, A. Farhan and A. Al-Salaymeh, *J. Ecol. Eng.*, 2019, **20**, 249–254.

10 P. Dwivedi, K. Sudhakar, A. Soni, E. Solomin and I. Kirpichnikova, *Case Stud. Therm. Eng.*, 2020, **21**, 100674.

This journal is © The Royal Society of Chemistry 2026

Energy Environ. Sci., 2026, **19**, 1124–1136 | **1135**

11 W. Li, Y. Shi, K. Chen, L. Zhu and S. Fan, *ACS Photonics*, 2017, **4**, 774–782.

12 L. Zhu, A. Raman, K. X. Wang, M. A. Anoma and S. Fan, *Optica*, 2014, **1**, 32–38.

13 G. Yıldız, M. O. Karaağaç, A. Ergün and M. Kayfeci, in *Handbook of Thermal Management Systems*, ed. F. Aloui, E. G. Varuvel and A. Sonthalia, Elsevier, 2023, pp. 623–638, DOI: 10.1016/B978-0-443-19017-9.00005-2.

14 R. Li, Y. Shi, M. Wu, S. Hong and P. Wang, *Nat. Sustainability*, 2020, **3**, 636–643.

15 Z. Li, T. Ma, F. Ji, H. Shan, Y. Dai and R. Wang, *ACS Energy Lett.*, 2023, **8**, 1921–1928.

16 X. Du, Z. Xie, H. Zhang, S. Jiang, X. Su and J. Fan, *Adv. Mater.*, 2025, **37**, 2505279.

17 H. Fang, S. Dang, P. Kumar, J. Wang, L. Xu, Y. Zhu, A. Almogbel, A. Albadri, S. De Wolf and Q. Gan, *Mater. Sci. Eng., R*, 2025, **165**, 101016.

18 J. Xu, P. Wang, Z. Bai, H. Cheng, R. Wang, L. Qu and T. Li, *Nat. Rev. Mater.*, 2024, **9**, 722–737.

19 J. Tan, X. Wang, W. Chu, S. Fang, C. Zheng, M. Xue, X. Wang, T. Hu and W. Guo, *Adv. Mater.*, 2024, **36**, 2211165.

20 Y. Zhang, D. K. Nandakumar and S. C. Tan, *Joule*, 2020, **4**, 2532–2536.

21 F. Zhao, H. Cheng, Z. Zhang, L. Jiang and L. Qu, *Adv. Mater.*, 2015, **27**, 4351–4357.

22 Y. Huang, H. Cheng, C. Yang, H. Yao, C. Li and L. Qu, *Energy Environ. Sci.*, 2019, **12**, 1848–1856.

23 Z. Ming, J. Zhang, W. Li, S. Wang, Y. Zhang, Z. Lu, T. Zhang, Z. Zhou, Y. Xia, Y. Zhang, X. Zhou and J. Xiong, *Adv. Mater.*, 2025, **37**, 2501809.

24 T. Xu, X. Ding, Y. Huang, C. Shao, L. Song, X. Gao, Z. Zhang and L. Qu, *Energy Environ. Sci.*, 2019, **12**, 972–978.

25 H. Wang, Y. Sun, T. He, Y. Huang, H. Cheng, C. Li, D. Xie, P. Yang, Y. Zhang and L. Qu, *Nat. Nanotechnol.*, 2021, **16**, 811–819.

26 C. Liu, S. Wang, X. Wang, J. Mao, Y. Chen, N. Fang and S.-P. Feng, *Energy Environ. Sci.*, 2022, **15**, 2489–2498.

27 X. Liu, H. Gao, J. E. Ward, X. Liu, B. Yin, T. Fu, J. Chen, D. R. Lovley and J. Yao, *Nature*, 2020, **578**, 550–554.

28 J. Tan, S. Fang, Z. Zhang, J. Yin, L. Li, X. Wang and W. Guo, *Nat. Commun.*, 2022, **13**, 3643.

29 X. Wen, Z. Sun, X. Xie, Q. Zhou, H. Liu, L. Wang, X. Qin and S. C. Tan, *Adv. Funct. Mater.*, 2024, **34**, 2311128.

30 Y. Zhang, Z. Yu, H. Qu, S. Guo, J. Yang, S. Zhang, L. Yang, S. Cheng, J. Wang and S. C. Tan, *Adv. Mater.*, 2024, **36**, 2208081.

31 T. Xu, X. Ding, H. Cheng, G. Han and L. Qu, *Adv. Mater.*, 2024, **36**, 2209661.

32 X. Zhang, H. Qu, X. Li, L. Zhang, Y. Zhang, J. Yang, M. Zhou, L. Suresh, S. Liu and S. C. Tan, *Adv. Mater.*, 2024, **36**, 2310219.

33 J. Bai, Y. Hu, T. Guang, K. Zhu, H. Wang, H. Cheng, F. Liu and L. Qu, *Energy Environ. Sci.*, 2022, **15**, 3086–3096.

34 L. Li, S. Feng, Y. Bai, X. Yang, M. Liu, M. Hao, S. Wang, Y. Wu, F. Sun, Z. Liu and T. Zhang, *Nat. Commun.*, 2022, **13**, 1043.

35 C. Guo, H. Tang, P. Wang, Q. Xu, H. Pan, X. Zhao, F. Fan, T. Li and D. Zhao, *Nat. Commun.*, 2024, **15**, 6100.

36 A. V. Delgado, F. Gonzalez-Caballero, R. J. Hunter, L. K. Koopal and J. Lyklema, *J. Colloid Interface Sci.*, 2007, **309**, 194–224.

37 J. Lin, Z. Zhang, X. Lin, X. Cai, S. Fu, X. Fang, Y. Ding, X. Wang, G. Sèbe and G. Zhou, *Adv. Funct. Mater.*, 2024, **34**, 2314231.

38 X. Wang, F. Lin, X. Wang, S. Fang, J. Tan, W. Chu, R. Rong, J. Yin, Z. Zhang, Y. Liu and W. Guo, *Chem. Soc. Rev.*, 2022, **51**, 4902–4927.

39 Y. Huang, K. Zhou, H. Cheng, T. He, H. Wang, J. Bai, C. Yang, T. Guang, H. Yao, F. Li, G. Hou, Z. Xu and L. Qu, *Adv. Funct. Mater.*, 2024, **34**, 2308620.

40 D. Zhao, H. Wang, Z. U. Khan, J. C. Chen, R. Gabrielsson, M. P. Jonsson, M. Berggren and X. Crispin, *Energy Environ. Sci.*, 2016, **9**, 1450–1457.

41 C.-G. Han, X. Qian, Q. Li, B. Deng, Y. Zhu, Z. Han, W. Zhang, W. Wang, S.-P. Feng, G. Chen and W. Liu, *Science*, 2020, **368**, 1091–1098.

42 Y. Hu, W. Yang, W. Wei, Z. Sun, B. Wu, K. Li, Y. Li, Q. Zhang, R. Xiao, C. Hou and H. Wang, *Sci. Adv.*, 2024, **10**, eadk4620.

43 Y. Chen, C. Ye, J. He, R. Guo, L. Qu and S. Tang, *Energy Environ. Sci.*, 2025, **18**, 6063–6075.

44 H. Cheng, Y. Huang, F. Zhao, C. Yang, P. Zhang, L. Jiang, G. Shi and L. Qu, *Energy Environ. Sci.*, 2018, **11**, 2839–2845.

45 D. K. Nandakumar, S. K. Ravi, Y. Zhang, N. Guo, C. Zhang and S. C. Tan, *Energy Environ. Sci.*, 2018, **11**, 2179–2187.

46 D. Shen, M. Xiao, G. Zou, L. Liu, W. W. Duley and Y. N. Zhou, *Adv. Mater.*, 2018, **30**, 1705925.

47 S. Guo, Y. Zhang, Z. Yu, M. Dai, X. Liu, H. Wang, S. Liu, J. J. Koh, W. Sun, Y. Feng, Y. Chen, L. Yang, P. Sun, G. Lu, C. Yu, W. Chen, S. De Wolf, Z. Wang and S. C. Tan, *Nat. Commun.*, 2025, **16**, 5267.

48 H. Jouhara, N. Khordehgah, S. Almahmoud, B. Delpech, A. Chauhan and S. A. Tassou, *Therm. Sci. Eng. Prog.*, 2018, **6**, 268–289.

49 G. Xue, Y. Xu, T. Ding, J. Li, J. Yin, W. Fei, Y. Cao, J. Yu, L. Yuan, L. Gong, J. Chen, S. Deng, J. Zhou and W. Guo, *Nat. Nanotechnol.*, 2017, **12**, 317–321.

50 D. K. Nandakumar, Y. Zhang, S. K. Ravi, N. Guo, C. Zhang and S. C. Tan, *Adv. Mater.*, 2019, **31**, 1806730.

51 D. Kraemer, Q. Jie, K. McEnaney, F. Cao, W. Liu, L. A. Weinstein, J. Loomis, Z. Ren and G. Chen, *Nat. Energy*, 2016, **1**, 16153.

1136 | *Energy Environ. Sci.*, 2026, **19**, 1124–1136

This journal is © The Royal Society of Chemistry 2026